Supplementary material: Variable modification of continental lithosphere during the Proterozoic Grenville Orogeny: Evidence from teleseismic P-wave tomography

Alistair Boyce[a,1,*], Ian D. Bastow[a], Eva. M. Golos[b], Stéphane Rondenay[c], Scott Burdick[d], Robert D. Van der Hilst[b]

[a]*Department of Earth Science and Engineering, Royal School of Mines, Prince Consort Road, Imperial College London, London, SW7 2BP, UK.*
[b]*Department of Earth, Atmospheric and Planetary Sciences, Massachusetts Institute of Technology, Cambridge, Massachusetts, USA.*
[c]*Department of Earth Science, University of Bergen, Allegaten 41, 5007 Bergen, Norway.*
[d]*Department of Geology, Wayne State University, Detroit, Michigan, 48202, USA.*

[*]Corresponding author
Email address: ab2568@cam.ac.uk (Alistair Boyce)
[1]Present Address : University of Cambridge, Department of Earth Science, Bullard Laboratories, Madingley Road, Cambridge, CB3 0EZ, UK.

Contents

1. The Global Dataset

Figures S1-S3 show the phases, earthquakes and stations used in the absolute arrival time inversion. Phase arrivals from USArray are available as CSS monthly files from the ANF http://anf.ucsd.edu/tools/events/download.php. Arrivals from the EHB Bulletin are available at http://www.isc.ac.uk/ehbbulletin/. P phase arrivals for networks in Canada added using AARM (Boyce et al., 2017) will be made available with a digital model file at http://ds.iris.edu/ds/products/emc/ or by contacting the corresponding author (email: ab2568@cam.ac.uk).

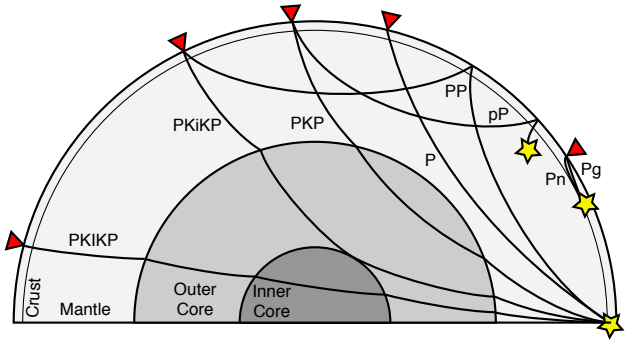

Figure S1: P-wave phases. Schematic of P-wave phases derived from the EHB Bulletin (see Li et al., 2008), USArray (see Burdick et al., 2017) and P-wave measurements from southeast Canada, used here for the first time in an absolute arrival-time inversion of North America.

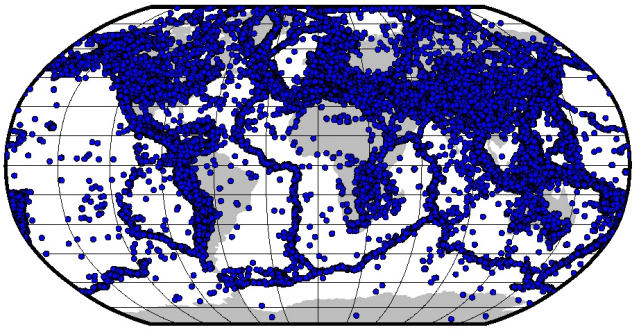

Figure S2: Earthquake map. Global earthquake map derived from the EHB Bulletin (see Li et al., 2008) and USArray (see Burdick et al., 2017), combined with teleseismic earthquakes recorded in southeast Canada.

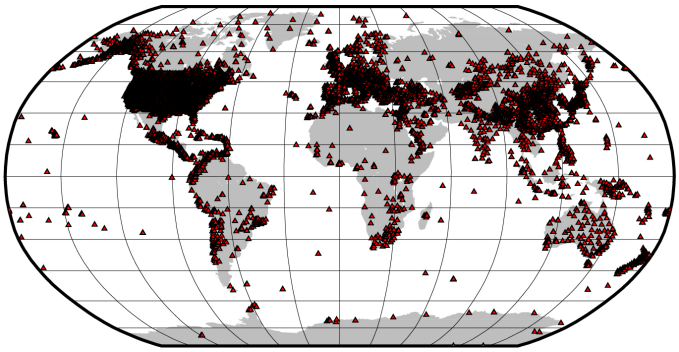

Figure S3: Seismograph stations. Global seismograph station map derived from the EHB Bulletin (see Li et al., 2008), USArray (see Burdick et al., 2017) and incorporated P-wave datasets from southeast Canada.

2. Direct P-wave Absolute Arrival-time Residuals

Figure S4 shows the direct-P phase absolute arrival-time residuals for the "EHB" database (Engdahl et al., 1998) used by Li et al. (2008), USArray Transportable Array (TA) picks of Burdick et al. (2017) and the southeast Canadian data added in this manuscript (see Section 2.2). We do not show residuals of any other phases used (e.g., Pn, Pg, pP, PP, PKP, PKiKP and PKIKP) which are primarily used to better constrain the crust and deep mantle.

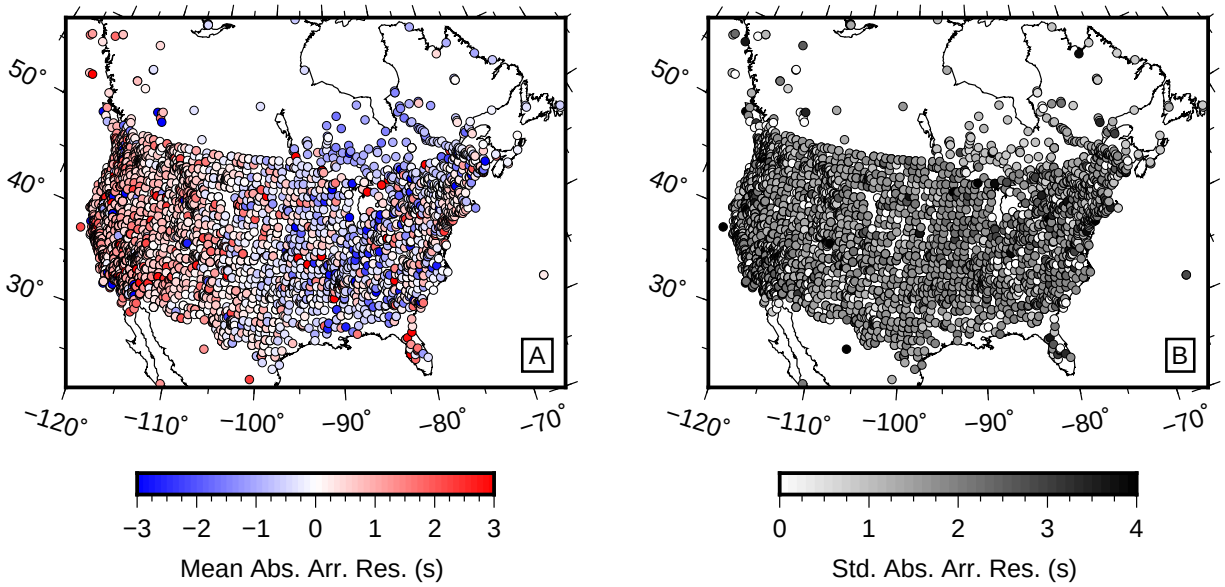

Figure S4: Direct-P phase absolute arrival-time residuals. Mean (A) and standard deviation (B) of the direct-P phase absolute arrival-time residuals for the "EHB" database (Engdahl et al., 1998) used by Li et al. (2008), USArray Transportable Array (TA) picks of Burdick et al. (2017) and the southeast Canadian data added in this manuscript (Figure 2).

3. Details of Southeast Canadian Datasets

For details of the southeast Canadian dataset and subsequent conversion to absolute arrival-time residuals see Boyce et al. (2016, 2017). Further data was sourced from the Canadian National Data centre, 'Superior Province Rifting Earthscope Experiment' and 'Teleseismic Studies in the Western Superior Transect' networks from the western Superior Province. The period $1997-2016$ yielded 446 $m_b > 5.5$ earthquakes with high SNR resulting in 4042 relative arrival-time picks from 34 stations. Results from this analysis are shown in Figure S5. Absolute arrival-times were calculated using the AARM method (see Boyce et al., 2017) resulting in 3766 picks from 408 earthquakes (Figure S6) from the western Superior dataset.

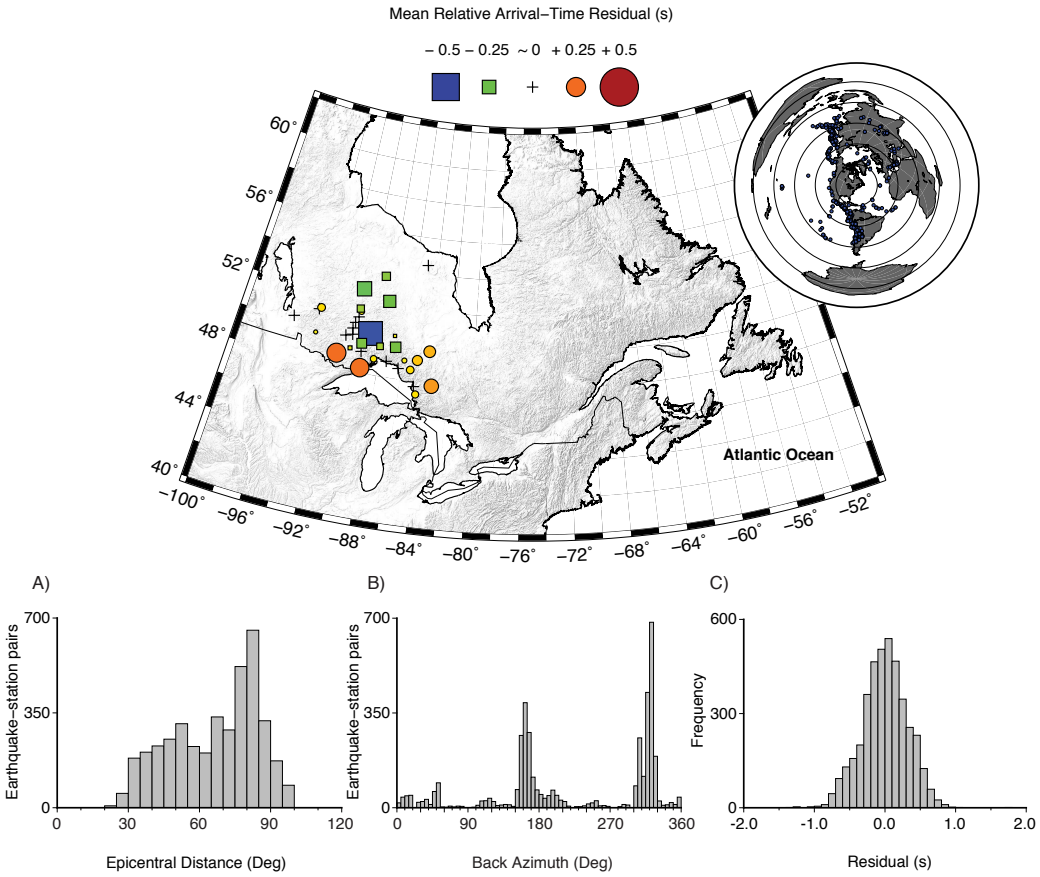

Figure S5: Relative arrival-time dataset for the western Superior. *ABOVE* - Mean relative arrival-time residual for 34 stations across the western Superior network. Early arrivals (faster) are represented by blue squares, later arrivals (slower) are shown as red circles. Inset globe shows the distribution of magnitude $m_b > 5.5$ earthquakes recorded with adequate SNR at ≥ 4 stations across the network between $1997 - 2016$. Concentric rings mark 30° increments in epicentral distance from the Superior Province in southeast Canada. *BELOW* - Plot of earthquake distribution with epicentral distance (A), earthquake frequency with backazimuth (B) and frequency distribution of residuals (C) for the P-wave dataset.

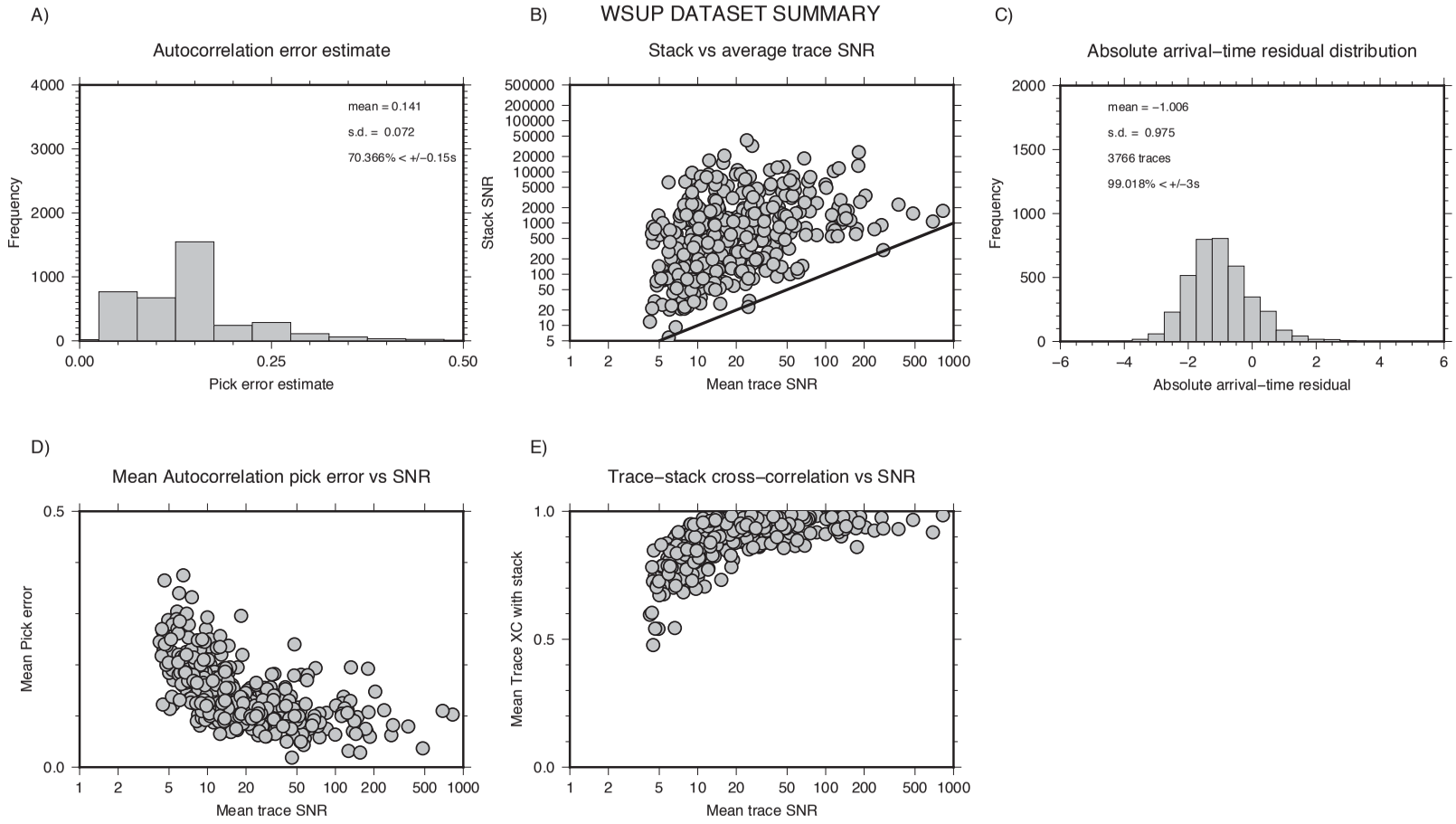

Figure S6: AARM overview (using cross-correlation scheme) for the western Superior network. (A): The autocorrelation pick error estimate for the entire dataset. (B): The variation in SNR of the final stacked trace against earthquake averaged SNR. The black line shows the line $y = x$. (C): The distribution of absolute arrival-time residuals for the dataset. (D): The variation of mean autocorrelation pick errors with earthquake averaged SNR. (E): Shows the mean cross-correlation coefficient of each trace with the stack as a function of earthquake-averaged SNR. For further detail on this figure see Boyce et al. (2017).

Additional data for southeast Canada were sourced from 34 stations in the QM-III network (Deep Structure of Three Continental Sutures Québec-Maine Array). Between 2012 and 2015, 297 $m_b > 5.5$ earthquakes resulted in 4142 relative arrival-time residuals (Figure S7). The AARM method (see Boyce et al., 2017) was used to calculate, 3599 absolute P-wave arrival-time picks from 250 earthquakes (Figure S8) for this dataset.

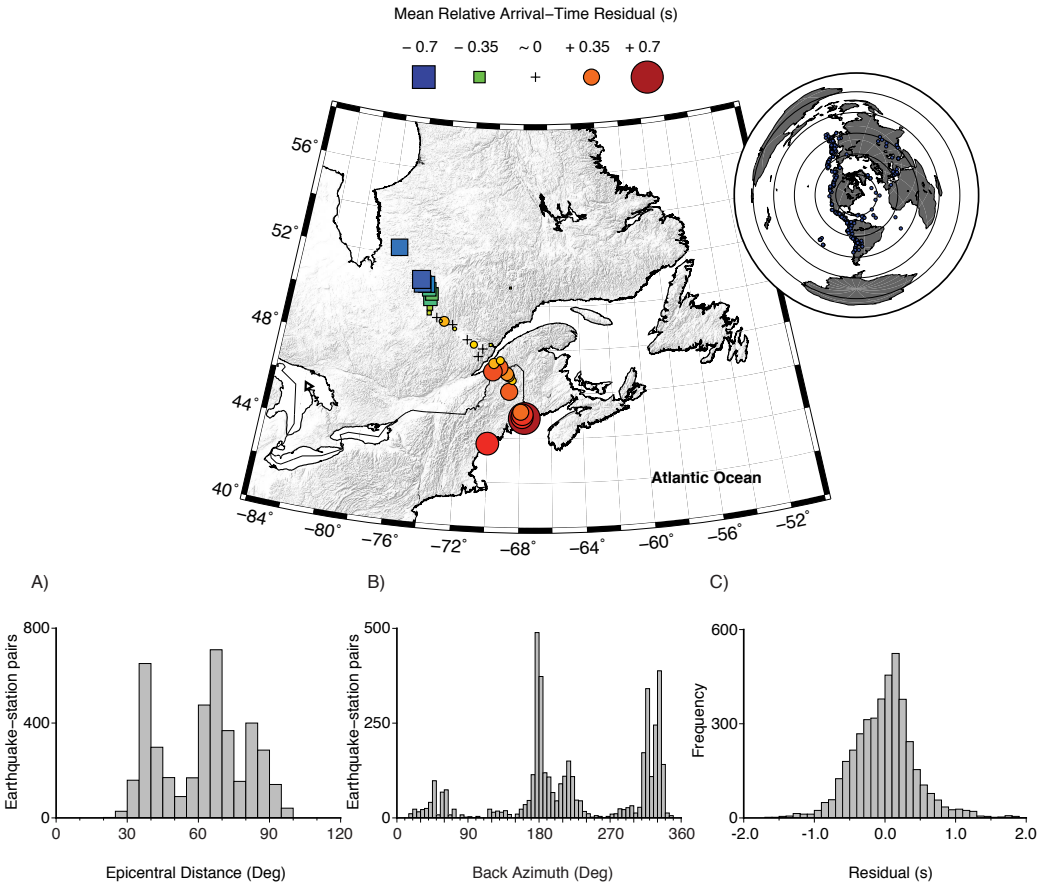

Figure S7: Relative arrival-time dataset for the QM-III network. *ABOVE* - Mean relative arrival-time residual for 34 stations across the QM-III network. Early arrivals (faster) are represented by blue squares, later arrivals (slower) are shown as red circles. Inset globe shows the distribution of magnitude $m_b > 5.5$ earthquakes recorded with adequate SNR at ≥ 4 stations across the network between $2012 - 2015$. Concentric rings mark 30° increments in epicentral distance from the Superior Province in southeast Canada. *BELOW* - Plot of earthquake distribution with epicentral distance (A), earthquake frequency with backazimuth (B) and frequency distribution of residuals (C) for the P-wave dataset.

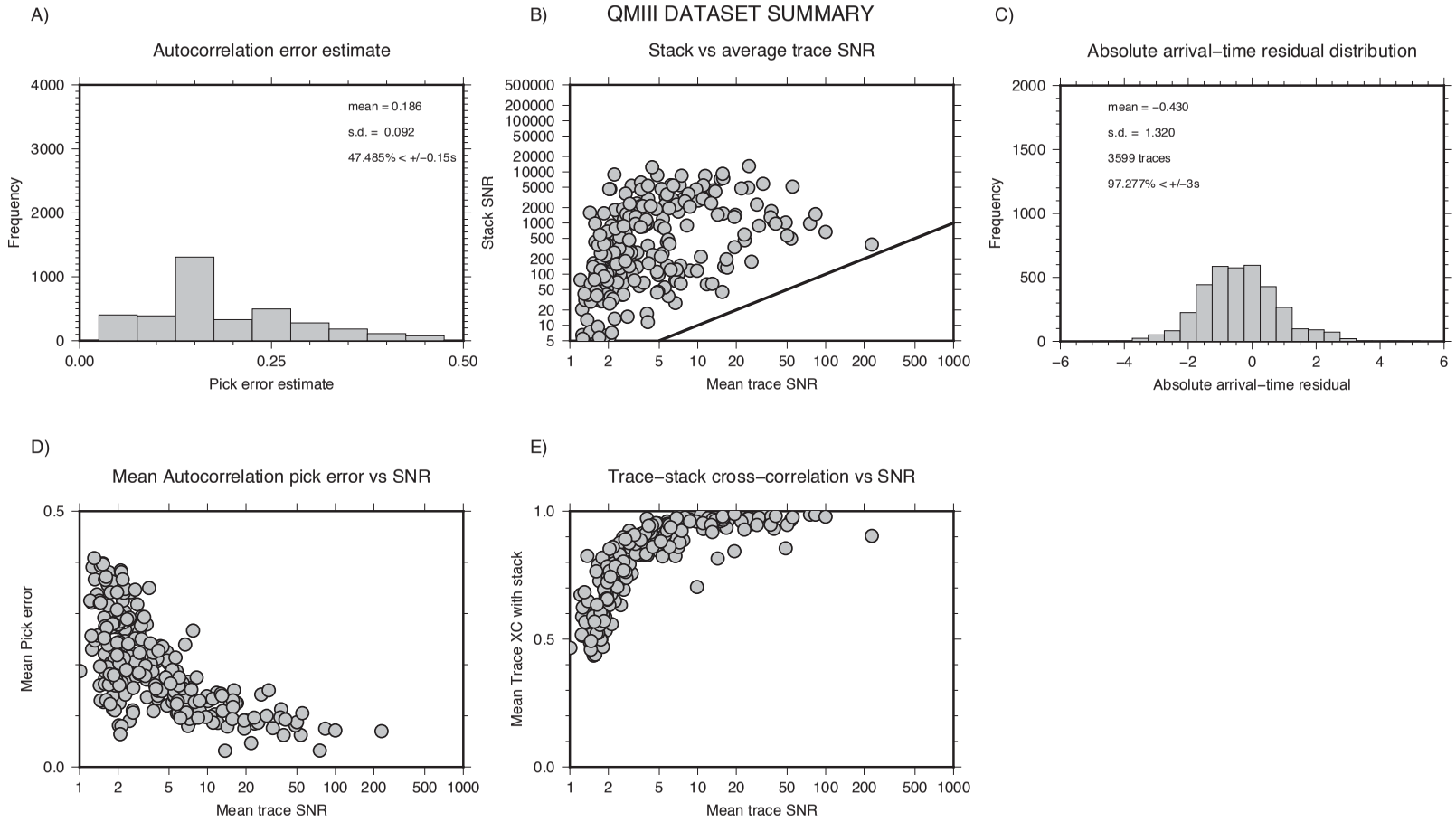

Figure S8: AARM overview (using cross-correlation scheme) for the QM-III network. (A): The autocorrelation pick error estimate for the entire dataset. (B): The variation in SNR of the final stacked trace against earthquake averaged SNR. The black line shows the line $y = x$. (C): The distribution of absolute arrival-time residuals for the dataset. (D): The variation of mean autocorrelation pick errors with earthquake averaged SNR. (E): Shows the mean cross-correlation coefficient of each trace with the stack as a function of earthquake-averaged SNR. For further detail on this figure see Boyce et al. (2017).

4. Adaptive Parameterization

Figure S9 shows the adaptively parameterized grid of cells for four depths ($100 - 400\,km$) in BBNAP19 plotted as fine black cells over the tomographic model. The velocity anomalies are plotted as in Figure 5 of the main manuscript.

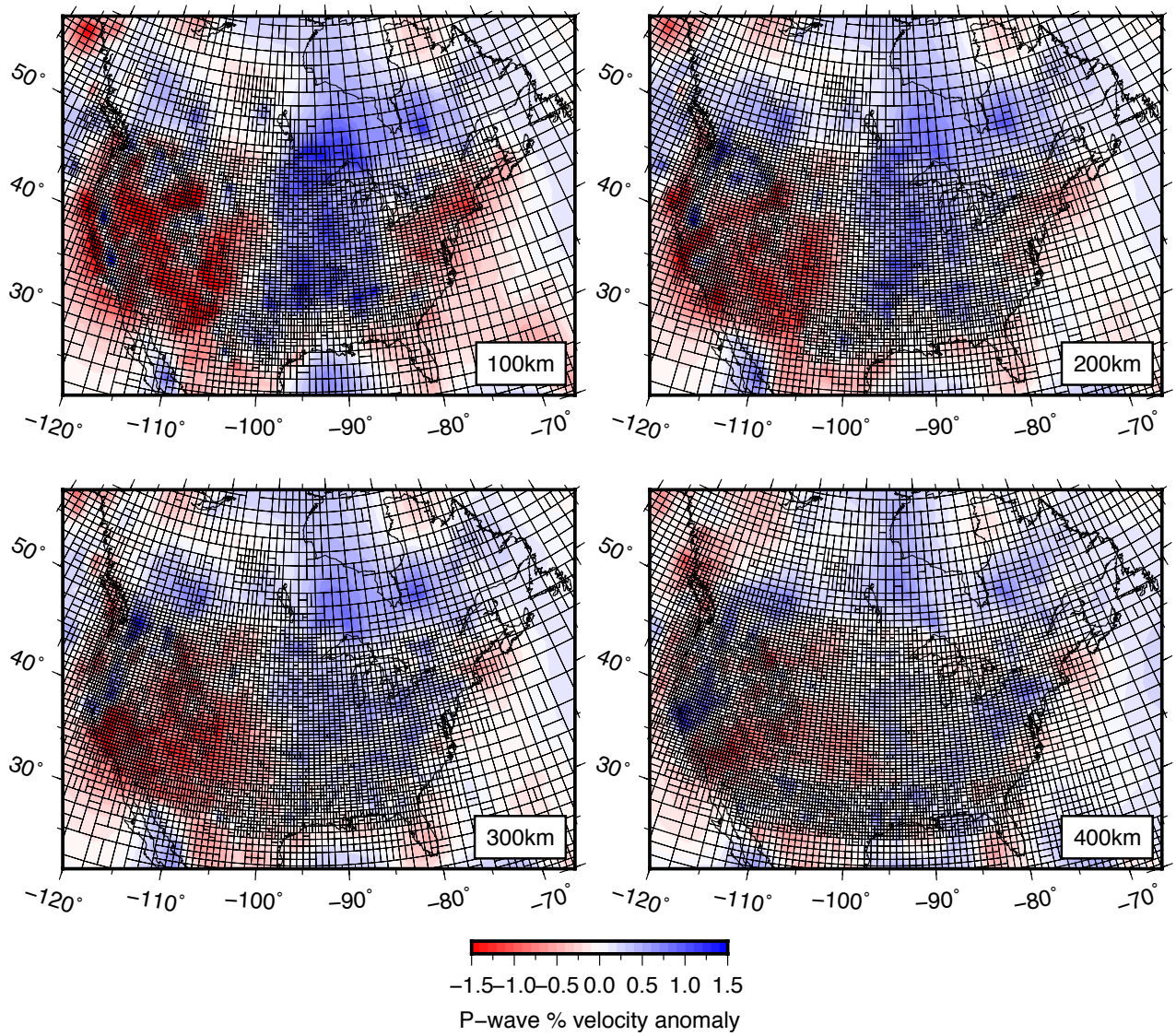

Figure S9: Adaptively parameterized grid. Adaptively parameterized grid of cells for four depths ($100 - 400\,km$) in BBNAP19 plotted as fine black cells over the tomographic model. The velocity anomalies are plotted as in Figure 5 of the main manuscript.

5. Trade-off Curve Approach

Figure S10 shows the trade-off curve approach used to determine vertical- and horizontal-gradient smoothing constraints in BBNAP19. We select our chosen model "E" based on proximity to the knee of the curve in the global parameterization and suitability for a North America-focused model given the abundance of North American data in BBNAP19 (e.g., Golos et al., 2018). We select the model damping in similar fashion.

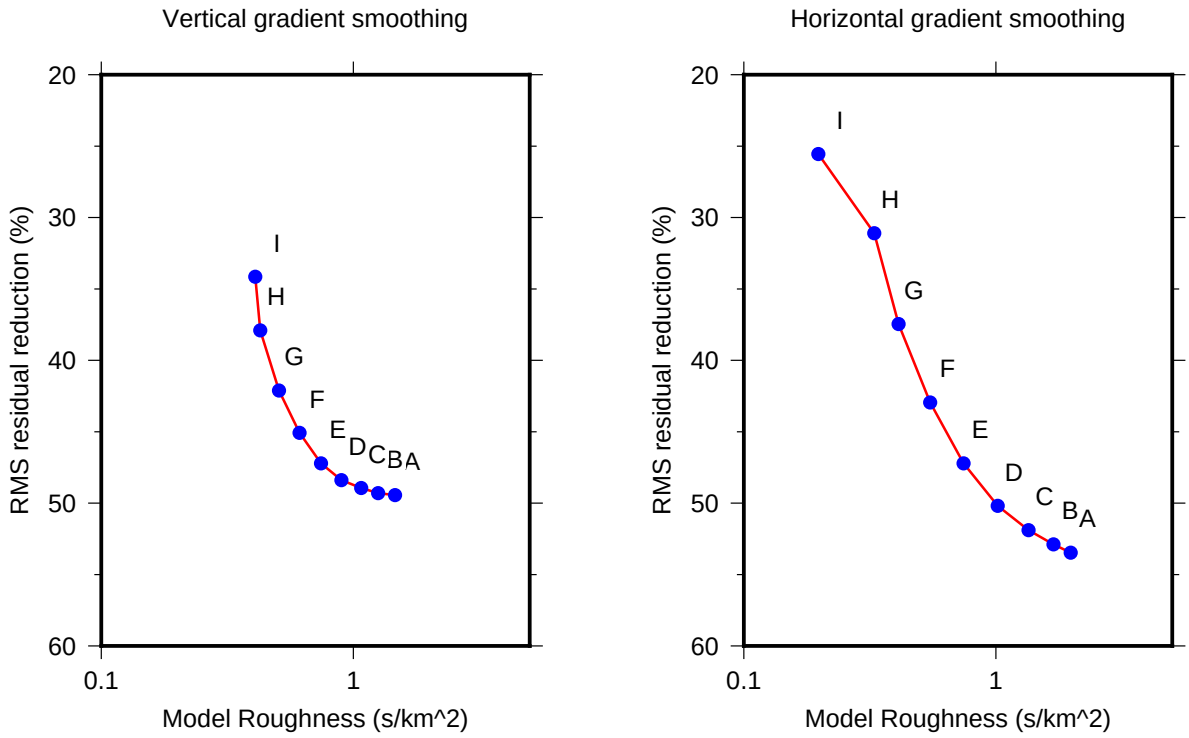

Figure S10: Smoothing trade-off curve. Trade-off curve used to determine vertical- and horizontal-gradient smoothing constraints in BBNAP19 in which root-mean-squared residual reduction (%) is plotted against model roughness (s/km^2). We choose model "E" which exhibits a RMS residual reduction of 47.2%.

6. Grenville Specific Resolution Tests

Figures S11-S13 show resolution tests specific for the Proterozoic Grenville Province of eastern North America in the BBNAP19 model. We construct synthetic velocity models with perturbations extending from the surface to increasing depths within the upper mantle ($50 - 200\,km$) to complement Figure 4 in the main manuscript. The input synthetic velocity anomaly varies linearly with latitude from $\delta V_P = -2.0\%$ to $\delta V_P = +2.0\%$ south-to-north in the Grenville Province. We use identical methodology to the resolution tests discussed in the main manuscript to assess recovery of these models.

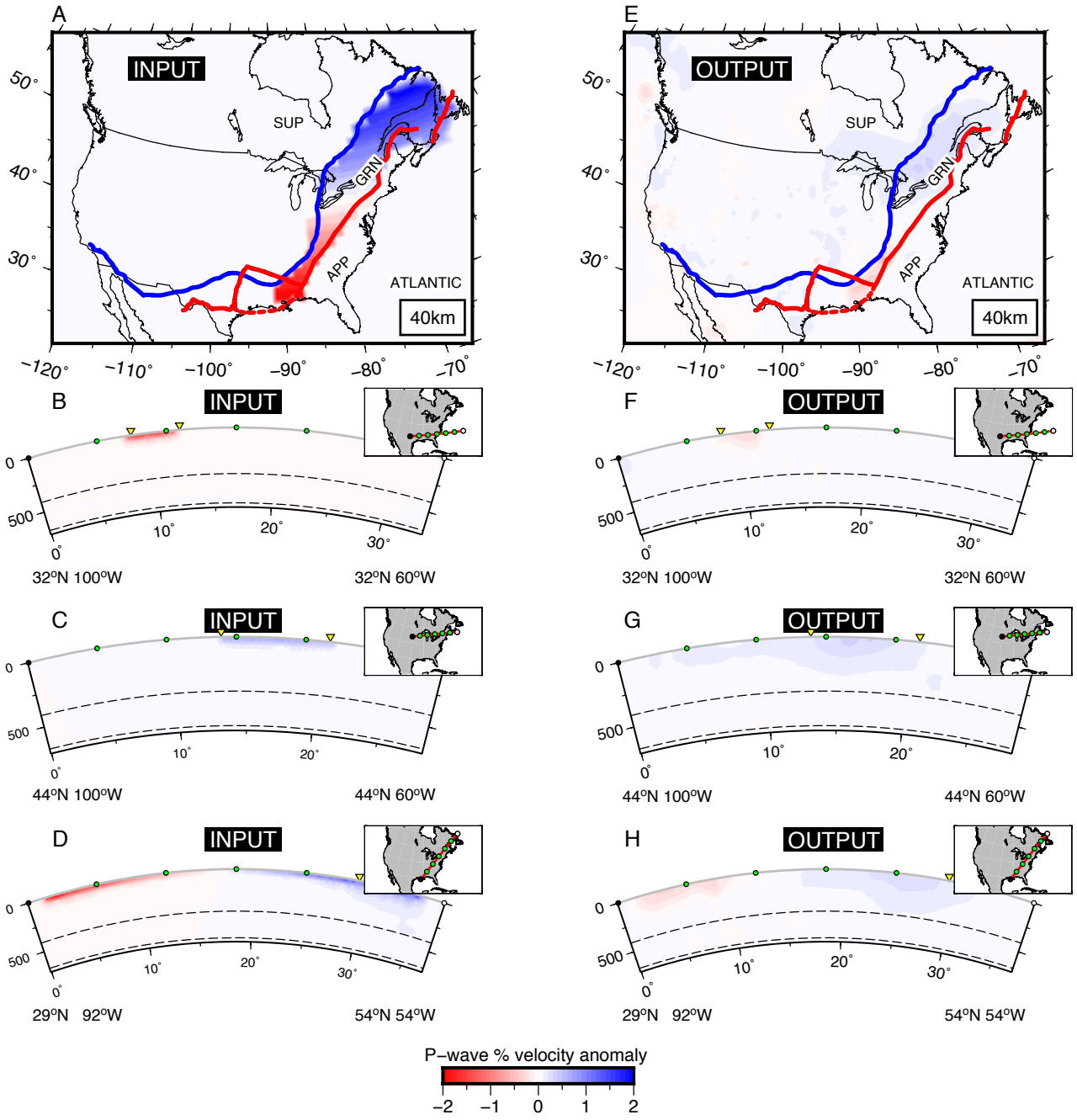

Figure S11: 50 km depth Grenville specific resolution test. Grenville specific resolution test showing recovery of a synthetic velocity anomaly linearly varying from δV_P = –2.0% to δV_P = +2.0% south-to-north in the Grenville Province at $\leq$ 50 km depth. A-D show the input velocity model, E shows the output model at 40 km depth, F-H show cross sections through the output model at 32°N, 44°N and parallel to the Grenville Province.

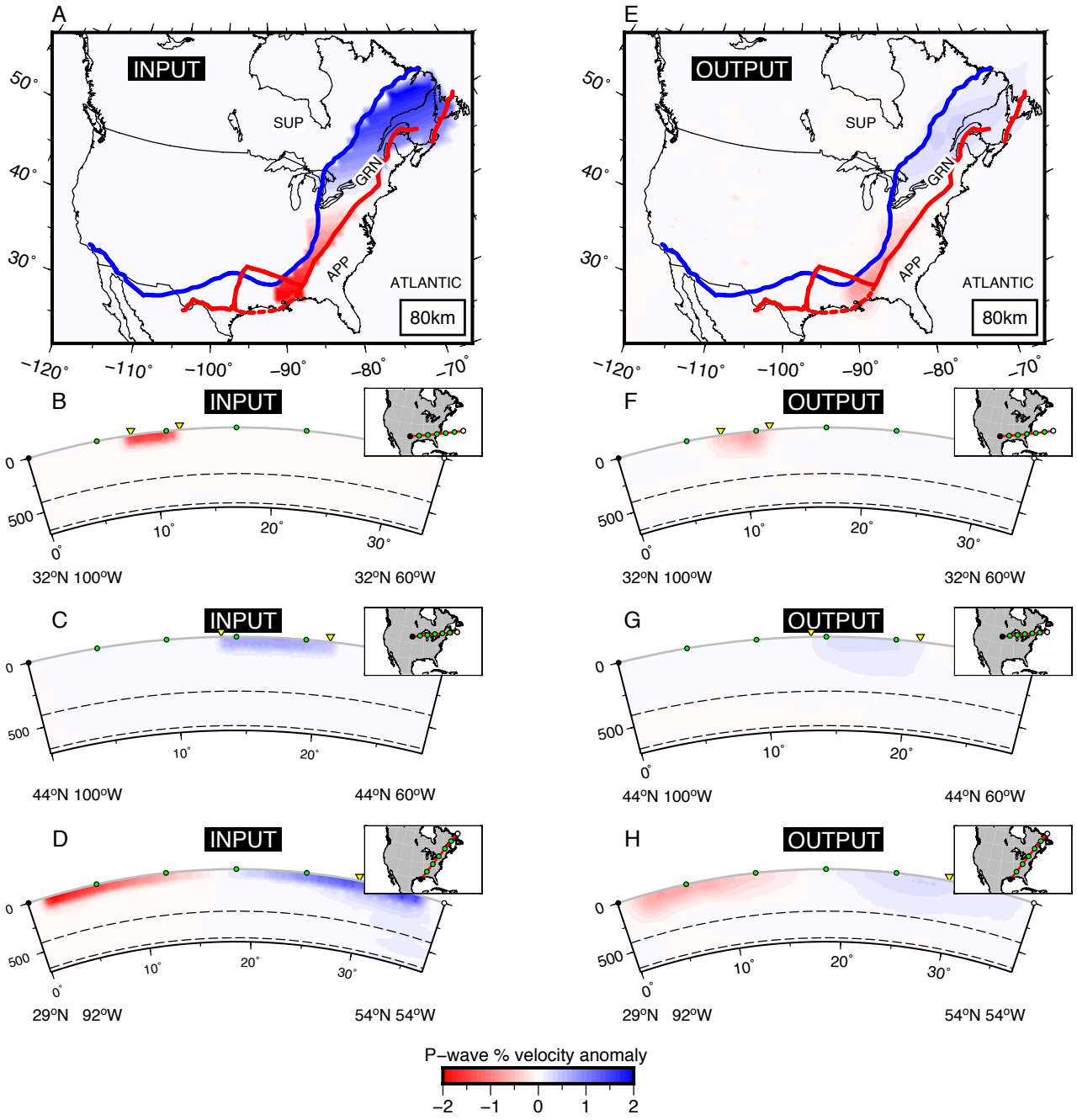

Figure S12: 100 km depth Grenville specific resolution test. Grenville specific resolution test showing recovery of a synthetic velocity anomaly linearly varying from δV_P = –2.0% to δV_P = +2.0% south-to-north in the Grenville Province at $\leq$100 km depth. A-D show the input velocity model, E shows the output model at 80 km depth, F-H show cross sections through the output model at 32°N, 44°N and parallel to the Grenville Province.

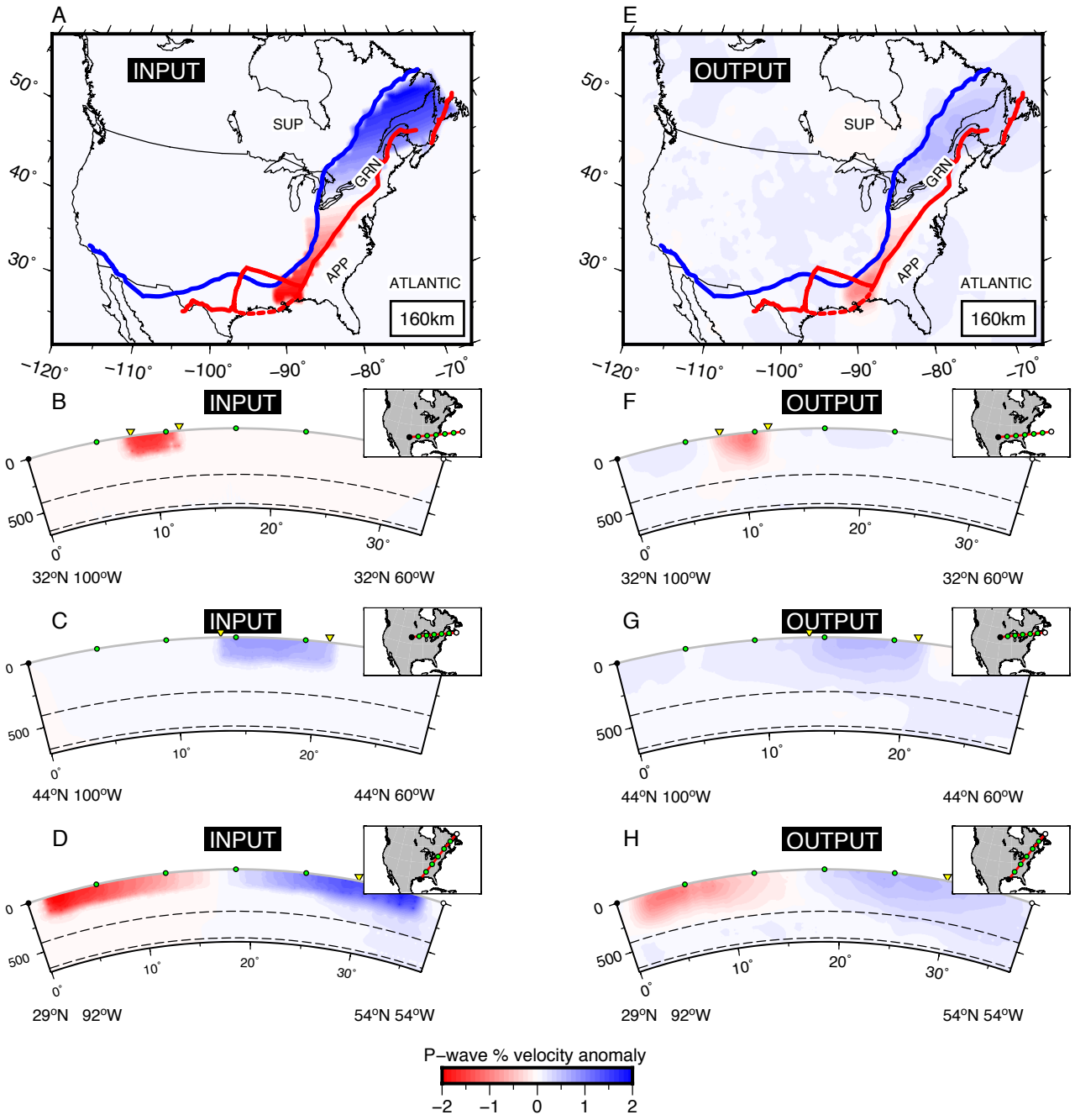

Figure S13: 200 km depth Grenville specific resolution test. Grenville specific resolution test showing recovery of a synthetic velocity anomaly linearly varying from $\delta V_P = -2.0\%$ to $\delta V_P = +2.0\%$ south-to-north in the Grenville Province at $\leq 200\,km$ depth. A-D show the input velocity model, E shows the output model at 160 km depth, F-H show cross sections through the output model at 32°N, 44°N and parallel to the Grenville Province.

7. Checkerboard Resolution Tests

Figures S14 and S15 show checkerboard resolution tests for North America in the BBNAP19 model. Although checkerboard resolution tests are an imperfect tool to assess model resolution, here we use the recovery of a 10° checkerboard to quantitatively assess the regions in which BBNAP19 resolves long wavelength features in the upper mantle following Burdick et al. (2014). We

compare m_0, the input 10° checkerboard model ($\delta V_P = \pm 2.0\%$ anomalies), with m, the recovered model to define the resolving power R as follows:

$$R = \frac{[(m - m_0)^T W (m - m_0)]^{1/2}}{(m_0^T W m_0)^{1/2}}. \quad (1)$$

W is a gaussian function that weights contributions from adjacent cells over the length-scale of the 10° checkerboard (Burdick et al., 2014). Regions in BBNAP19 are well resolved in which $R > 0.2$. The results of this analysis are used to define the grey regions of Figure 5 in the main manuscript.

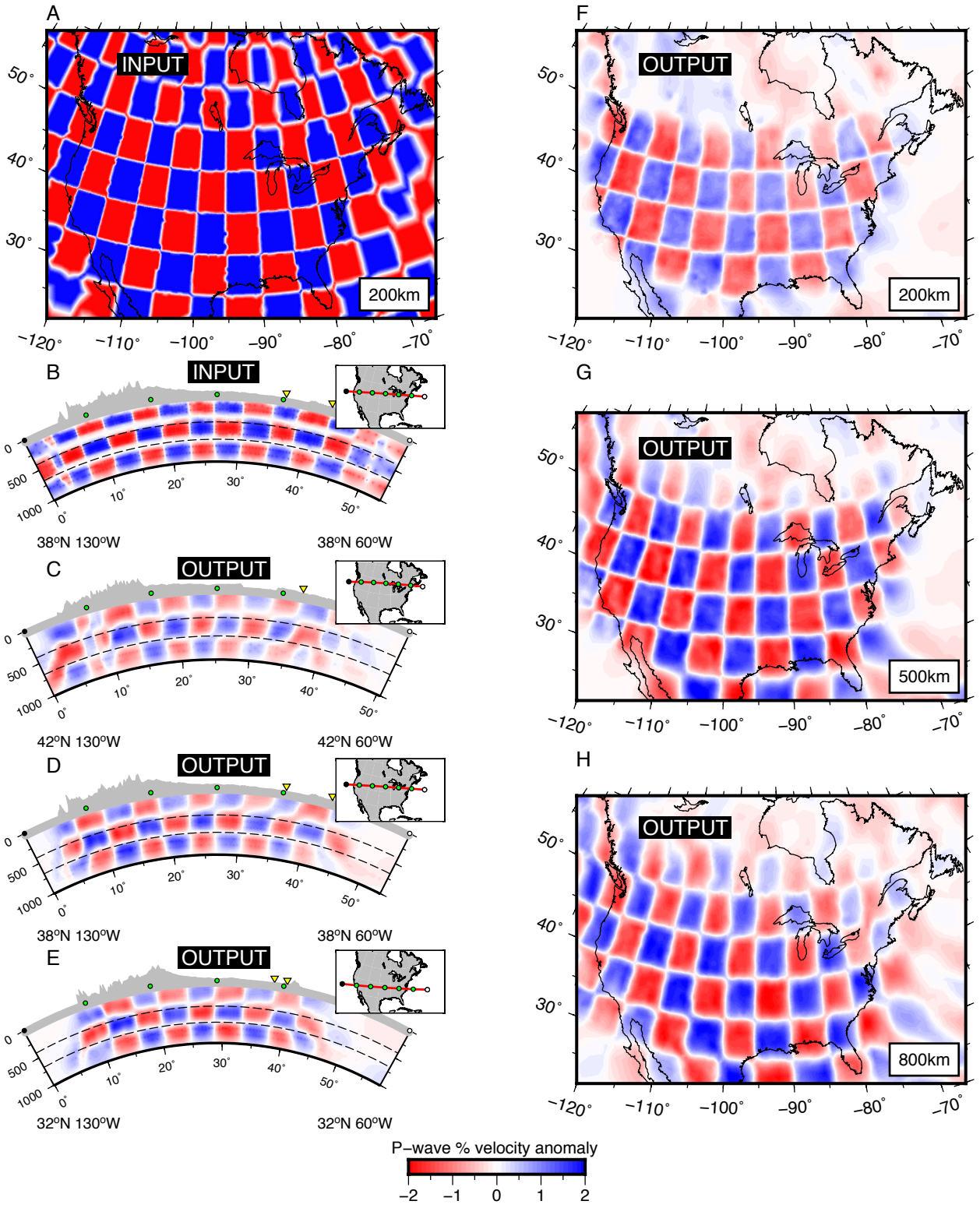

Figure S14: 5° checkerboard resolution tests. Checkerboard resolution tests showing recovery of 5° velocity anomalies distributed throughout North America. A and B show the input velocity $\delta V_P = \pm 2.0\%$ anomalies, C-E show cross sections at 42°N, 38°N and 32°N through the output model. F-H show the output model at 200 km, 500 km and 800 km depth.

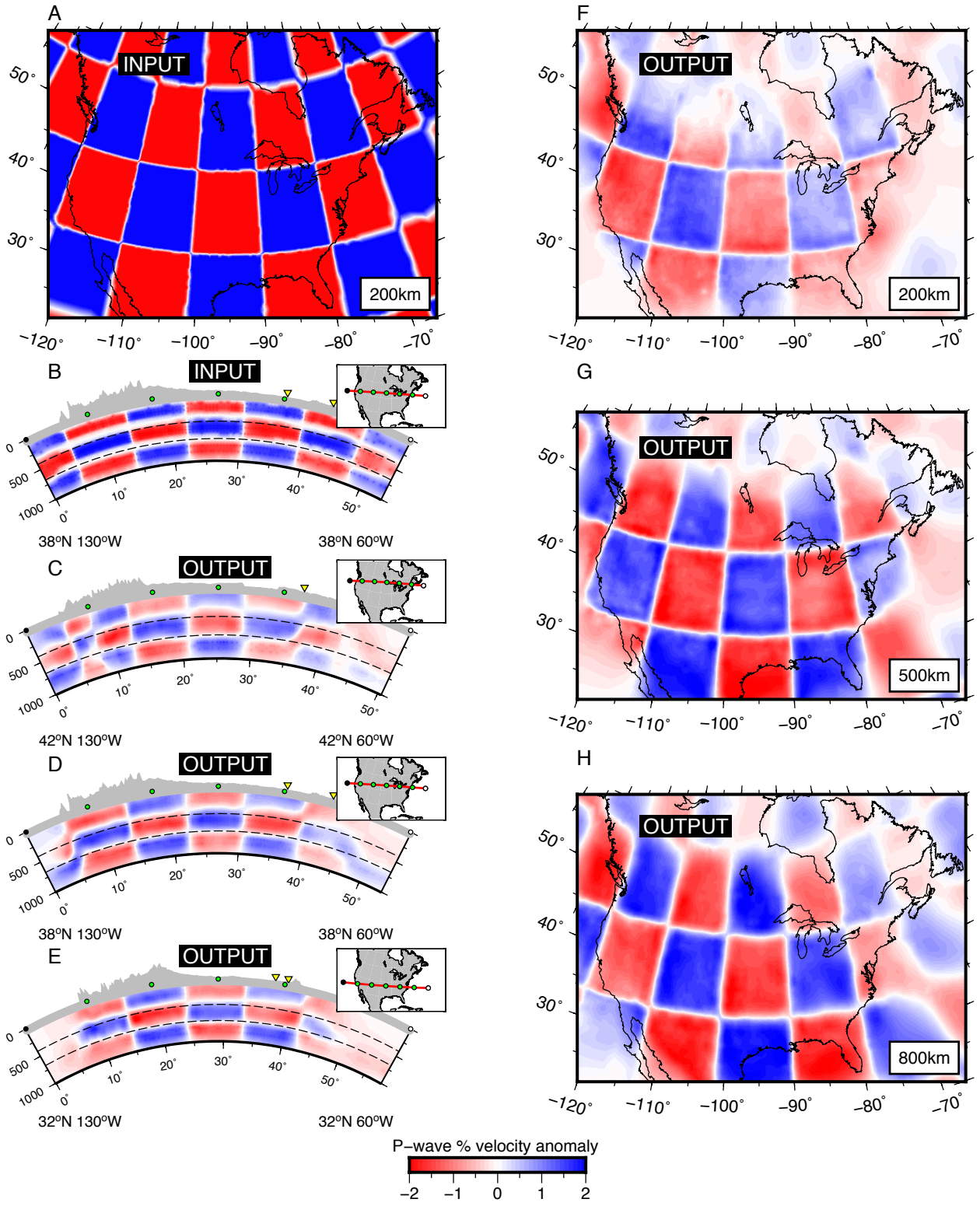

Figure S15: 10° checkerboard resolution tests. Checkerboard resolution tests showing recovery of 10° velocity anomalies distributed throughout North America. A and B show the input velocity $\delta V_P = \pm 2.0\%$ anomalies, C-E show cross sections at 42°N, 38°N and 32°N through the output model. F-H show the output model at 200 km, 500 km and 800 km depth.

8. Lateral Scales of Resolution

Figure S16 shows synthetic (A, E) and checkerboard (B-D, F-H) resolution tests for North America in the BBNAP19 model. Synthetic input models (A, E) are plotted in color in the background with 0.1% velocity contours (grey) from the recovered model plotted in the foreground. This is used to visually estimate the amount of lateral smearing present at the Grenville and Appalachian fronts in the lithosphere. In the U.S. Grenville, lateral smearing appears to be less than $50\,km$. In the Canadian Grenville lateral smearing appears to be on the order $\sim 50\,km$ perhaps increasing to $\geq 100\,km$ in Labrador in the far northeast.

Output checkerboard resolution tests (Figure S16B-D, F-H) are plotted to investigate the minimum resolvable scale of regularly-shaped distinct velocity anomalies in the Grenville Province region. Identical methodology to the resolution tests discussed in the main manuscript is used. In regions where the shape of velocity anomalies is distinctly recovered, rather than smeared laterally (producing a diagonal streaking effect), we propose that the minimum resolvable scale is half the width of the input checkers. At 35°N in the U.S. Grenville, one degree of longitude equates to $\sim 90\,km$, whilst at 50°N in the Canadian Grenville, one degree of longitude equates to $\sim 70\,km$. Upon visual inspection, 2° velocity anomalies are recovered in the U.S. Grenville, which equates to an isolated velocity anomaly minimum resolvable scale of $\sim 90\,km$. This value is comparable with the average station spacing of the USArray TA of $\sim 70\,km$. In Canada the outline of $5 - 7.5°$ input checkers is recovered but this increases towards Labrador and in the northern Superior Province. In the Canadian Grenville investigated here, we estimate a minimum resolvable scale of $\sim 175 - 260\,km$. This increase largely reflects the increase in station spacing in Canada. The width of the Grenville varies from $150 - 700\,km$ south-to-north suggesting our long-wavelength ($\gg 1000\,km$) wavespeed observations within the Grenville are robust.

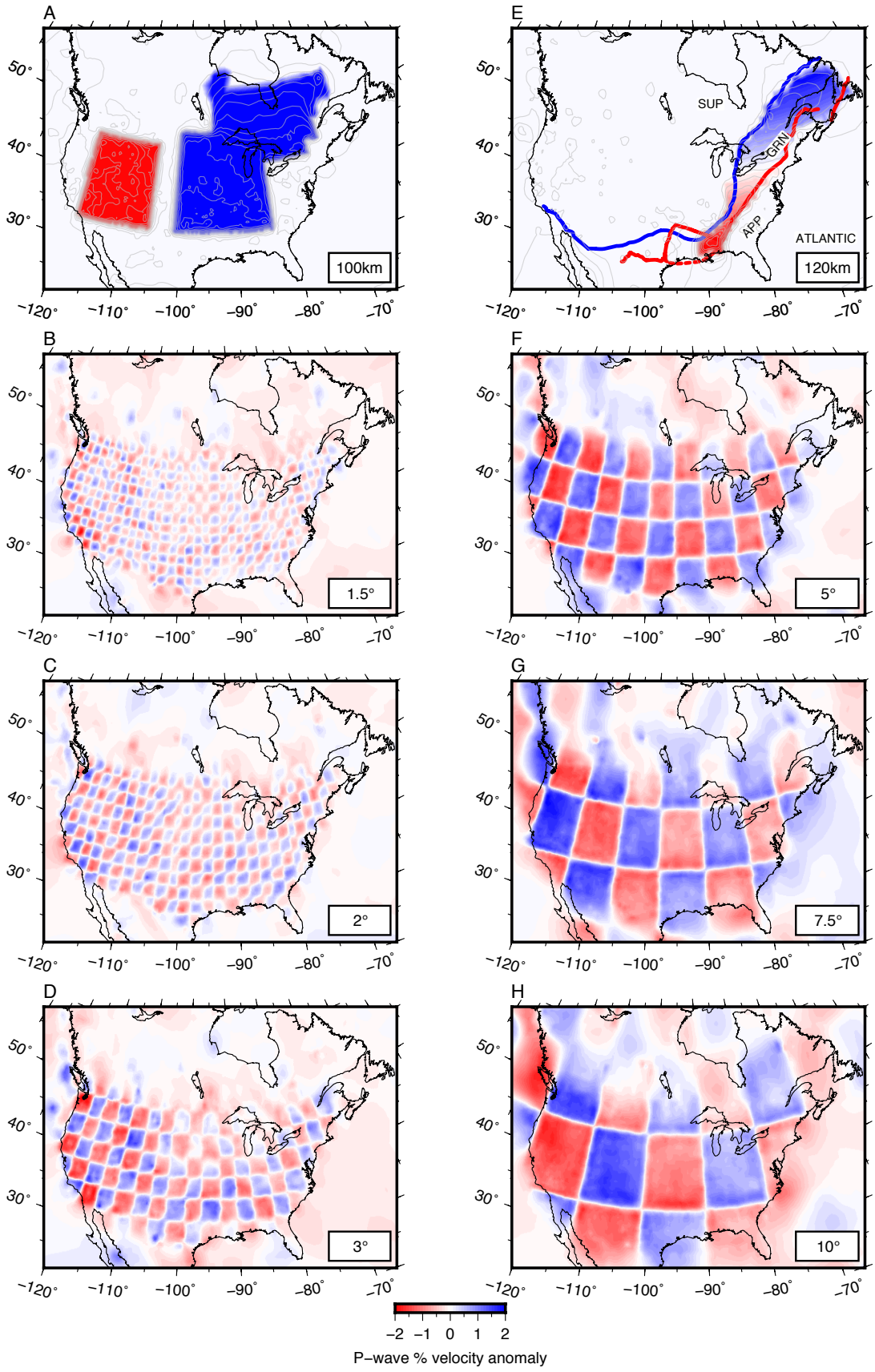

Figure S16: Lateral scale of resolution tests. Figure to visually estimate the lateral scale of resolution throughout eastern North America. A, E show the input from synthetic resolution tests (Figures 3A and 4A - main manuscript) plotted in color in the background with 0.1% velocity contours (grey) from the recovered (output) model (Figures 3E and 4E - main manuscript) plotted in the foreground. Using identical methodology to the resolution tests discussed in the main manuscript, B-D and F-H plot the recovered checkerboards for input anomalies ($\pm 2\% \delta V_P$) of increasing spatial scales varying from $1.5 - 10°$.

References

Boyce, A., Bastow, I.D., Darbyshire, F.A., Ellwood, A.G., Gilligan, A., Levin, V., Menke, W., 2016. Subduction beneath Laurentia modified the eastern North American cratonic edge: Evidence from P wave and S wave tomography. J. Geophys. Res. 121, 5013–5030. doi:10.1002/2016JB012838.

Boyce, A., Bastow, I.D., Rondenay, S., Van der Hilst, R.D., 2017. From relative to absolute teleseismic travel-times: the Absolute Arrival-time Recovery Method (AARM). Bull. Seis. Soc. Am. 107, 2511—-2520. doi:10.1785/0120170021.

Burdick, S., Van der Hilst, R.D., Vernon, F.L., Martynov, V., Cox, T., Eakins, J., Karasu, G.H., Tylell, J., Astiz, L., Pavlis, G.L., 2014. Model Update January 2013: Upper Mantle Heterogeneity beneath North America from Travel-Time Tomography with Global and USArray Transportable Array Data. Seis. Res. Lett. 85, 77–81. doi:10.1785/0220130098.

Burdick, S., Vernon, F.L., Martynov, V., Eakins, J., Cox, T., Tytell, J., Mulder, T., White, M.C., Astiz, L., Pavlis, G.L., Van der Hilst, R.D., 2017. Model Update May 2016: Upper-Mantle Heterogeneity beneath North America from Travel-Time Tomography with Global and USArray Data. Seis. Res. Lett. 88, 319–325. doi:10.1785/0220160186.

Engdahl, E.R., Van der Hilst, R.D., Buland, R., 1998. Global teleseismic earthquake relocation with improved travel times and procedures for depth determination. Bull. Seis. Soc. Am. 88, 722–743.

Golos, E.M., Fang, H., Yao, H., Zhang, H., Burdick, S., Vernon, F., Schaeffer, A., Lebedev, S., Van der Hilst, R.D., 2018. Shear Wave Tomography Beneath the United States Using a Joint Inversion of Surface and Body Waves. J. Geophys. Res. 123, 5169–5189. doi:10.1029/2017jb014894.

Li, C., Van der Hilst, R.D., Engdahl, R., Burdick, S., 2008. A new global model for P wave speed variations in Earth's mantle. Geochem. Geophys. Geosyst. 9. doi:10.1029/2007GC001806.